Supplementary Information for

Hydrogen-Stabilized Dual-Phase Architecture Enables Exceptional Ductility in Refractory Molybdenum Nanowires

Yuxuan Hou[1,‡], Haixuan Cao[1,‡], Huayu Peng[1], Ruilong Huang[1], Huaiyuan Wang[1], Bochun Yu[1], Peili Zhao[1], Shuangfeng Jia[1], He Zheng[1,*] and Jianbo Wang[1,2,*]

[1]School of Physics and Technology, Center for Electron Microscopy, MOE Key Laboratory of Artificial Micro- and Nano-structures, and Institute for Advanced Studies, Wuhan University, Wuhan 430072, China

[2]Core Facility of Wuhan University, Wuhan 430072, China

E-mail: zhenghe@whu.edu.cn; wang@whu.edu.cn

This file includes:

Supplementary Note 1. Knock-on and thermal effects resulting from e-beam irradiation.

The maximum energy that 300 keV electrons can transfer to Mo atoms is 8.9 eV. Given that the threshold displacement energy at 300 K in bulk Mo is about 27 eV[1], the knock-on effect could be suppressed within the interior of NWs in the current experiments. Besides, the impact of e-beam irradiation on hydrogen atoms remains limited due to two primary factors: (i) the inherent scattering cross section of hydrogen atoms is very small, which further decreases with increasing primary electron energy[2], and (ii) the metallic behavior of molybdenum and its hydrides enables rapid dissipation of energy transferred via inelastic collisions between primary electrons and atoms[3].

According to the Fisher's Model[4], the maximum temperature increase ΔT induced by the e-beam irradiation is ~10.2 K in Mo NWs, which has negligible influence on the deformation mechanisms.

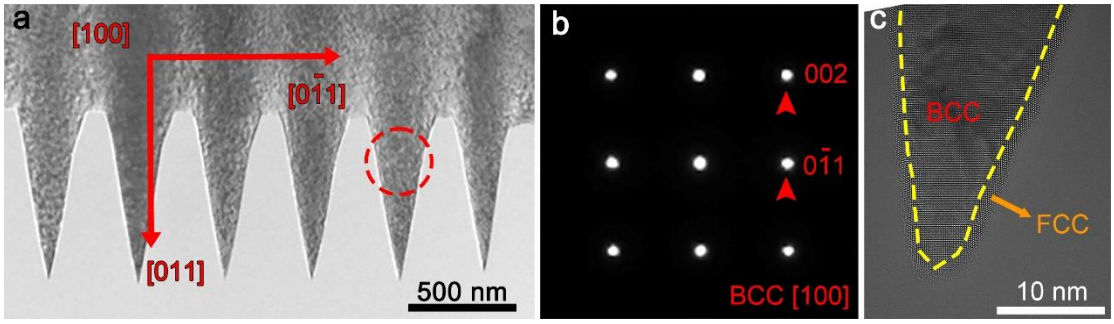

Supplementary Fig. 1 Structural characterization of pristine Mo nanopillars and a Mo nanotip with dual-phase structure. a, Transmission electron microscopy (TEM) image of vertically aligned Mo nanopillars fabricated via FIB. **b,** Selected area electron diffraction (SAED) pattern acquired from the red circle area in **a**, showing its BCC crystal structure along the [100] zone axis. These nanopillars can be further processed into individual NWs through a thermal welding method. **c,** Dual-phase structure in a Mo nanotip after 40 minutes of e-beam irradiation. The interior region maintains the original BCC structure, while a clear FCC phase nucleates at the surface.

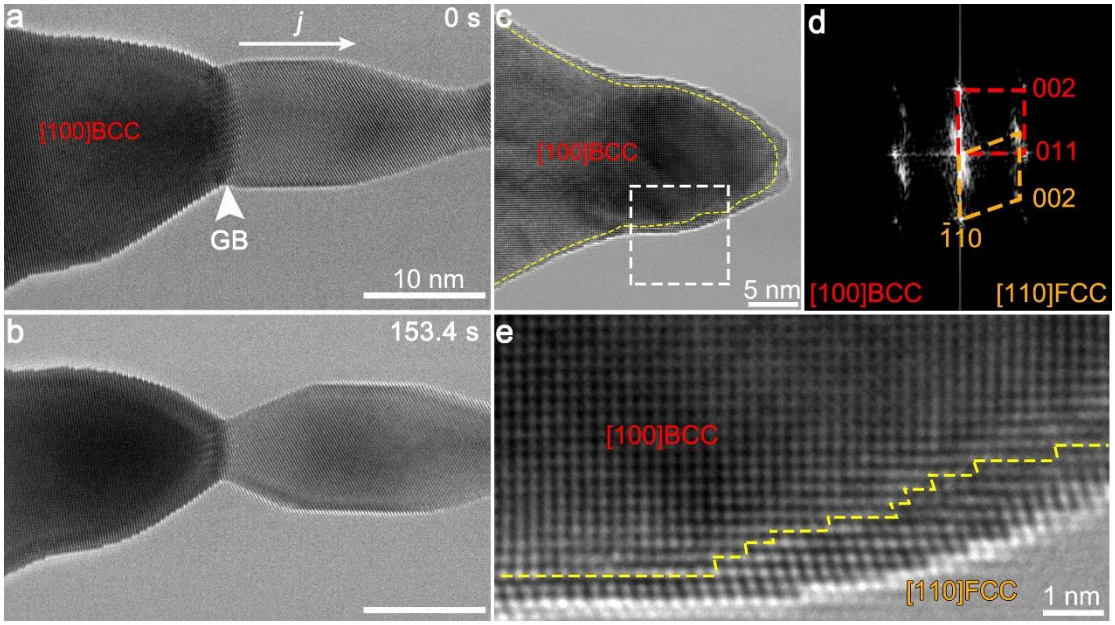

Supplementary Fig. 2 Dual-phase structure induced by high-density electric current. a-b, TEM images showing the application of a bias voltage of 0.4 V to an initial Mo NW. The current density reaches an ultra-high value of ~10^9 A/cm², leading

to significant diameter reduction and eventual fracture at the GB via electromigration. **c-d,** Structural characterization of the fractured NW tip, revealing a thin FCC surface layer. The FFT pattern obtained from the white dashed area in **c** displays two sets of diffraction spots that correspond to BCC and FCC lattices. **e,** Magnified HRTEM image showing the clear atomic-scale interface between the BCC and FCC phases.

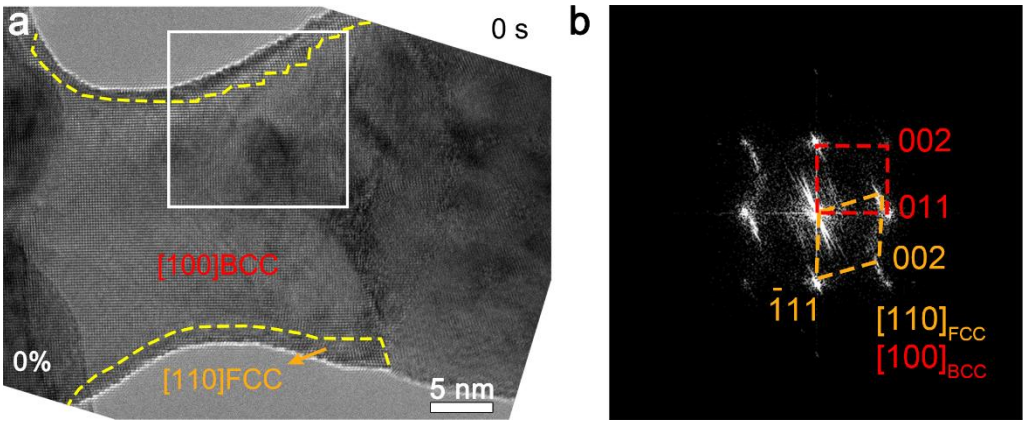

Supplementary Fig. 3 Structural characterization of the FCC/BCC dual-phase Mo NW. a, The TEM image showing the initial dual-phase NWs. **b,** The FFT pattern acquired from the white-square area in **a.**

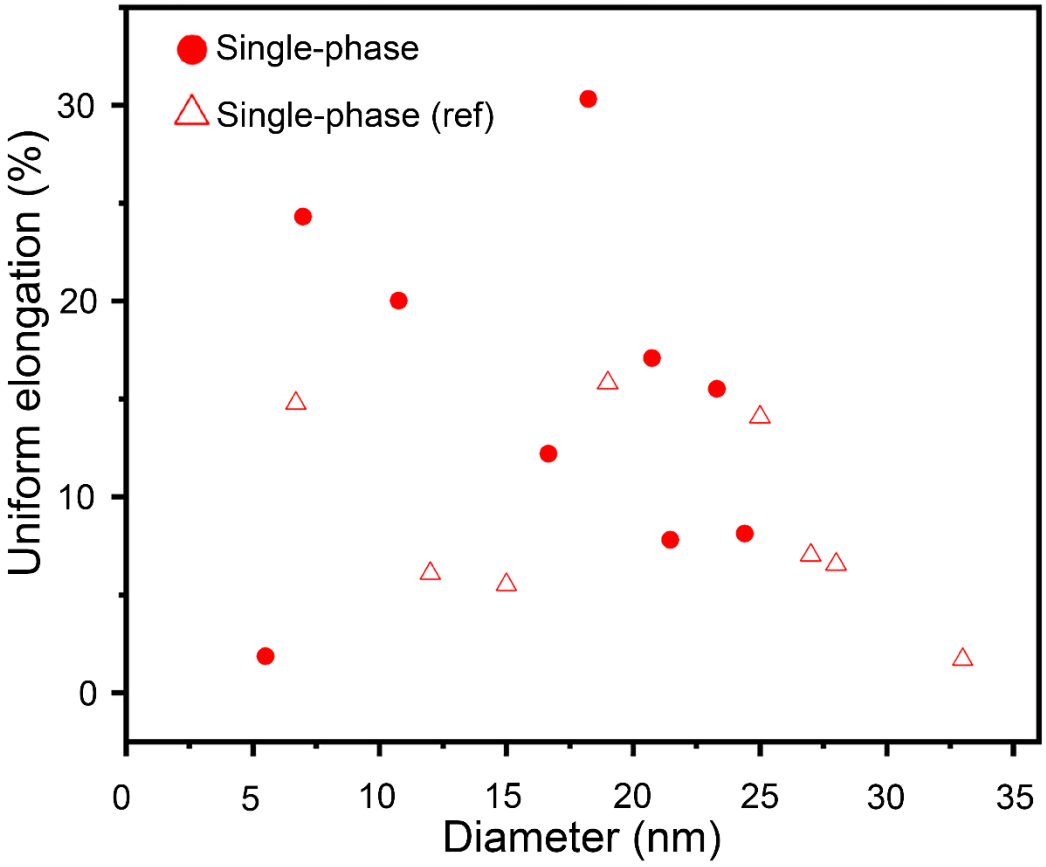

Supplementary Fig. 4 Statistical analysis of ductility in BCC Mo NWs. The uniform elongation versus the NW diameter for both experimentally measured data (red circles) and previously reported values[5] (red triangles), showing no strong dependence of uniform elongation on diameter within this size range.

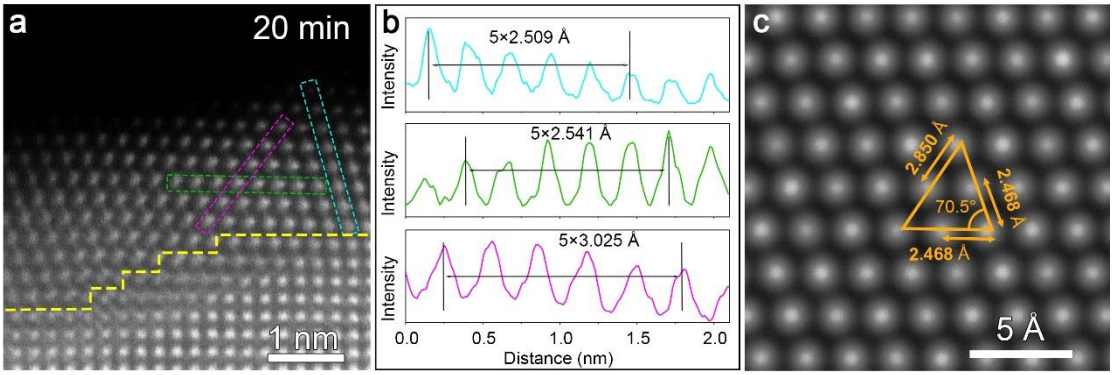

Supplementary Fig. 5 Lattice parameter measurements of the FCC phase.

a, HAADF-STEM image presenting the lattice structure of the same region shown in Fig. 2a after 20 minutes of irradiation. **b,** Line intensity profiles corresponding to the colored regions in **a**. The measured spacings of the two neighboring atoms on $(\bar{1}11)$, $(1\bar{1}1)$, and (001) plane are 2.541 Å, 2.509 Å, and 3.025 Å, respectively. **c,** Simulated HAADF image of the FCC structure with a lattice constant of 4.03 Å.

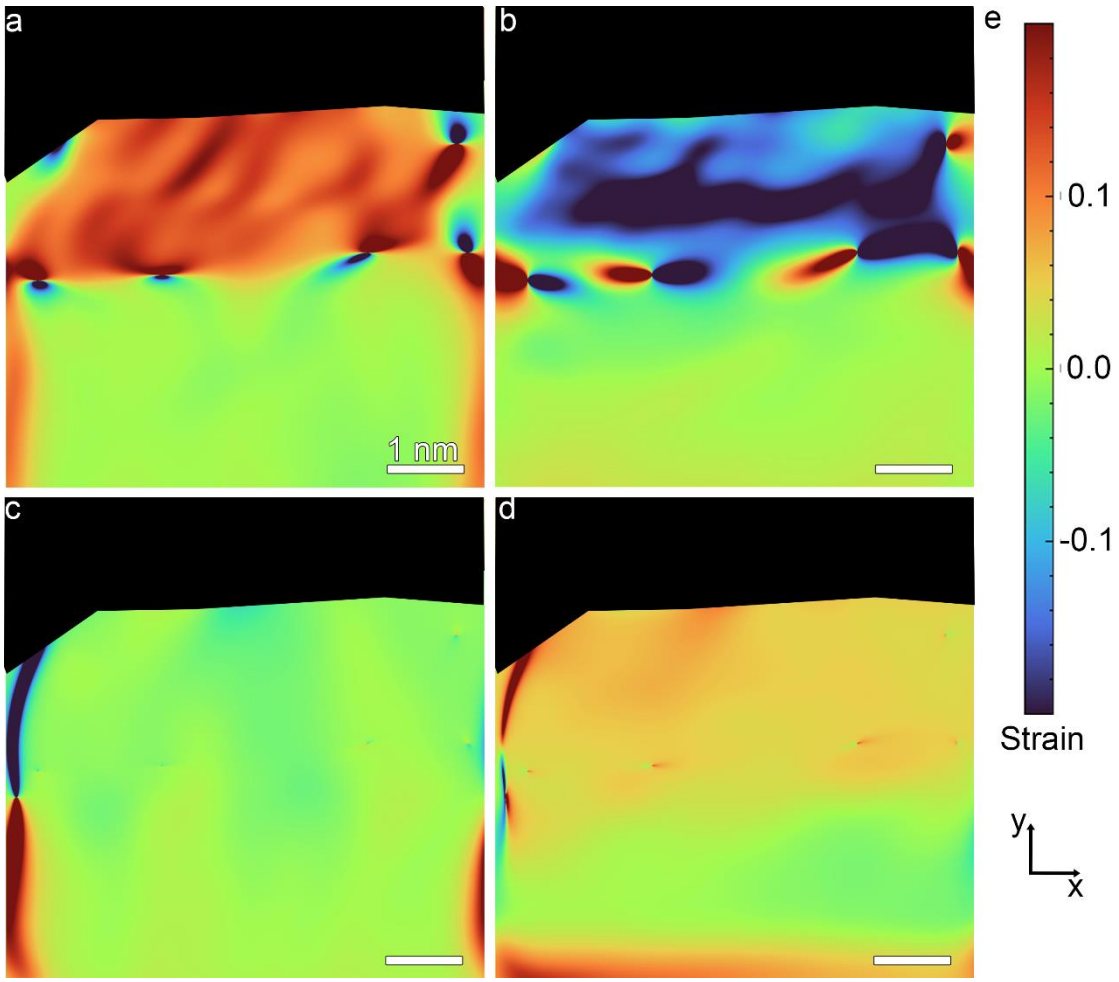

Supplementary Fig. 6 Geometrical phase analysis of Fig. 2b. a-d, The horizontal strain ε_{xx}, shear strain components ε_{xy}, ε_{yx} and the vertical strain ε_{yy}, respectively. **e,** The color scale bar represents the strain magnitude. The largest shear strain in the BCC phase is lower than 0.01, unlikely to trigger the phase transformation, which requires

significant shear strain (~ 0.051)[6] in the parent phase.

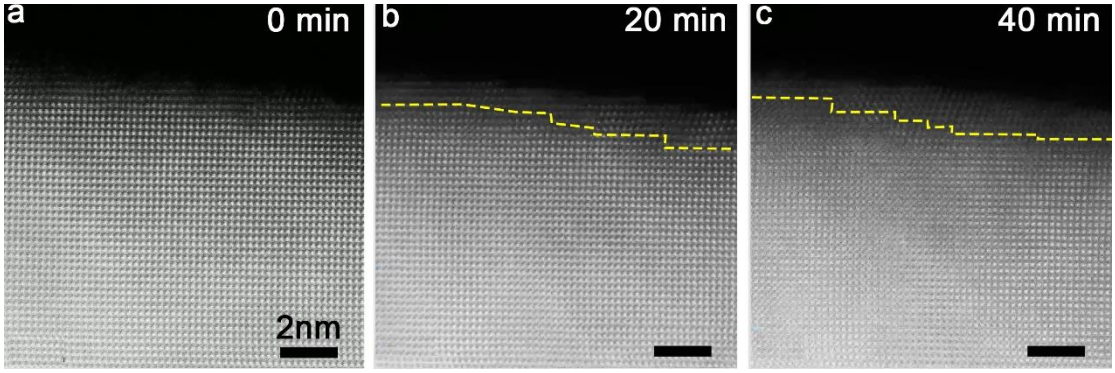

Supplementary Fig. 7 Localized BCC-to-FCC phase transformation within the surface area. a-c, HAADF-STEM images of BCC-to-FCC phase transformation under e-beam irradiation. The FCC phase nucleates from the surface and gradually propagates into the NW interior. However, only a limited thickness FCC layer forms after the prolonged irradiation from 20 to 40 minutes.

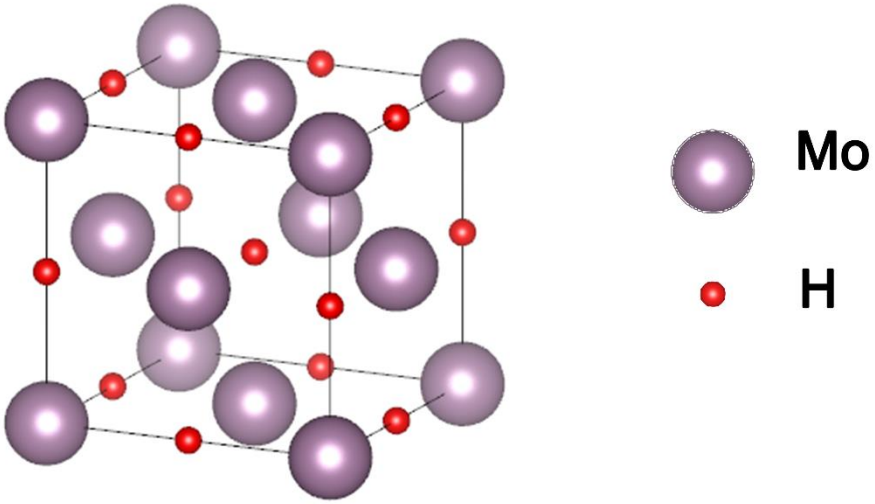

Supplementary Fig. 8 Schematic illustration of FCC-MoH structure. The FCC-Mo lattice (purple spheres) with hydrogen atoms (red) occupying the octahedral interstitial

sites, with the lowest-energy state.

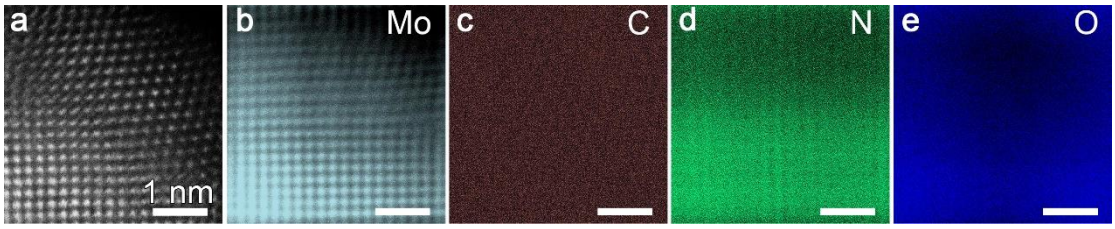

Supplementary Fig. 9 HAADF image and corresponding EDS mapping within a dual-phase area. a-e, The results show no obvious accumulation of light elements within the FCC phase.

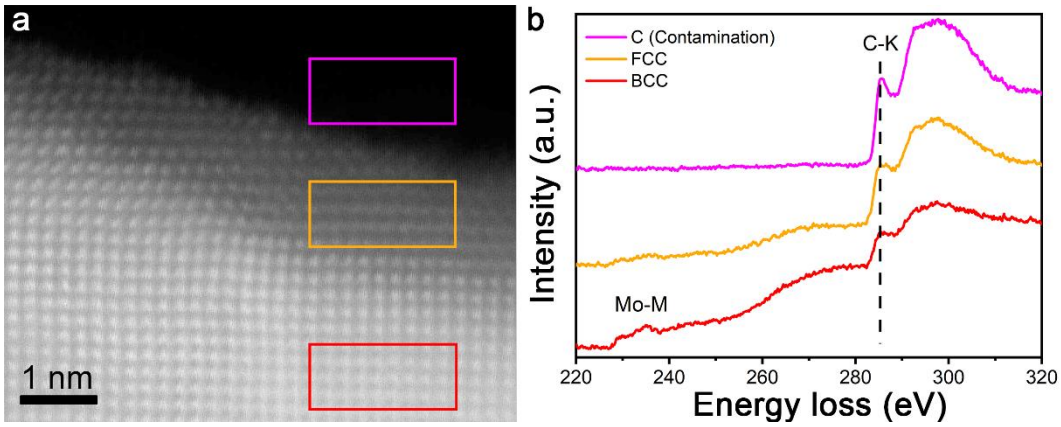

Supplementary Fig. 10 EELS evidence ruling out carbon as the transformation cause. a, HAADF-STEM image with colored rectangles indicating the BCC (red), FCC (orange), and vacuum (blue) regions. **b,** EELS spectra showing the C K-edge and Mo M-edge of the corresponding regions in **a**. The carbon signal is present in both BCC and FCC phases. This indicates that the presence of carbon is not the determining factor for the phase transformation from BCC to FCC.

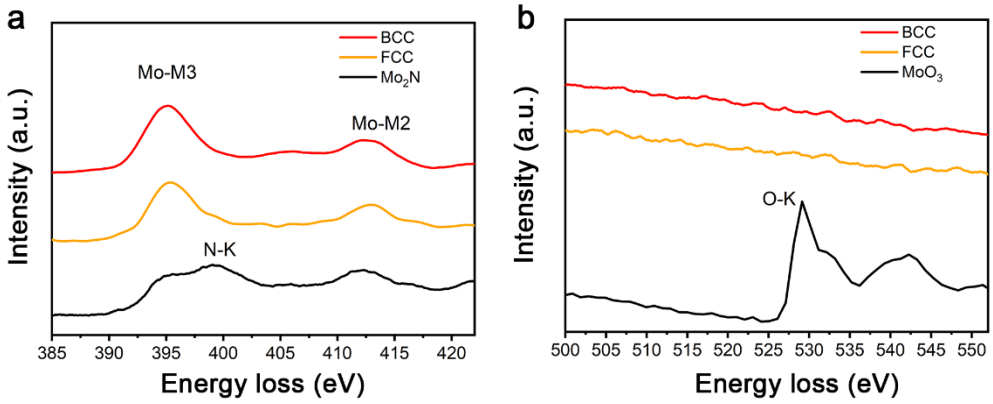

Supplementary Fig. 11 No detectable nitrogen and oxygen in the FCC-Mo phase revealed by EELS analysis. a-b, EELS spectra of the Mo-M, N-K and O-K edges, respectively, where nitrogen and oxygen edges are not detected.

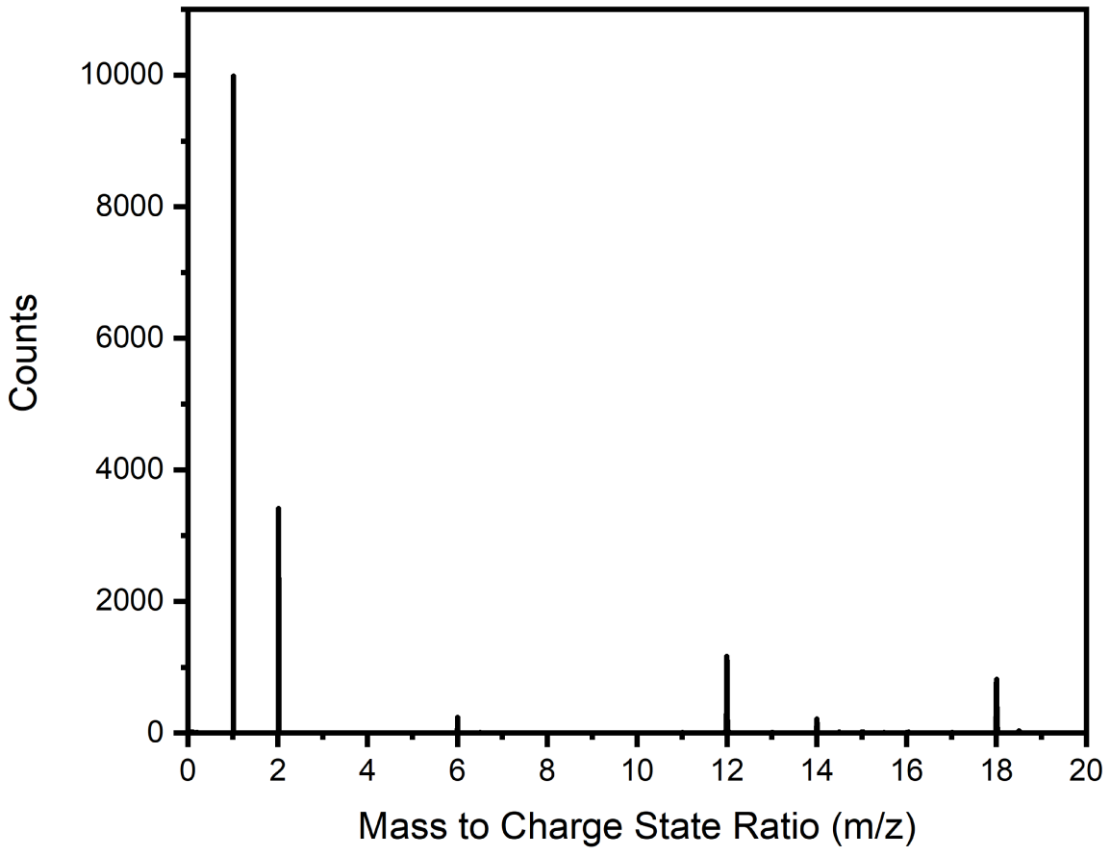

Supplementary Fig. 12 APT mass spectrum of the Mo sample. The spectrum reveals dominant peaks at m/z = 1 and m/z =2, identified as atomic and molecular H ions, respectively. The peak at m/z = 2 represents field-desorbed molecular H. The high

abundance of atomic H relative to molecular H, combined with the tip-localized enrichment shown in Fig. 2g-h, provides direct evidence for H incorporation in the Mo lattice.

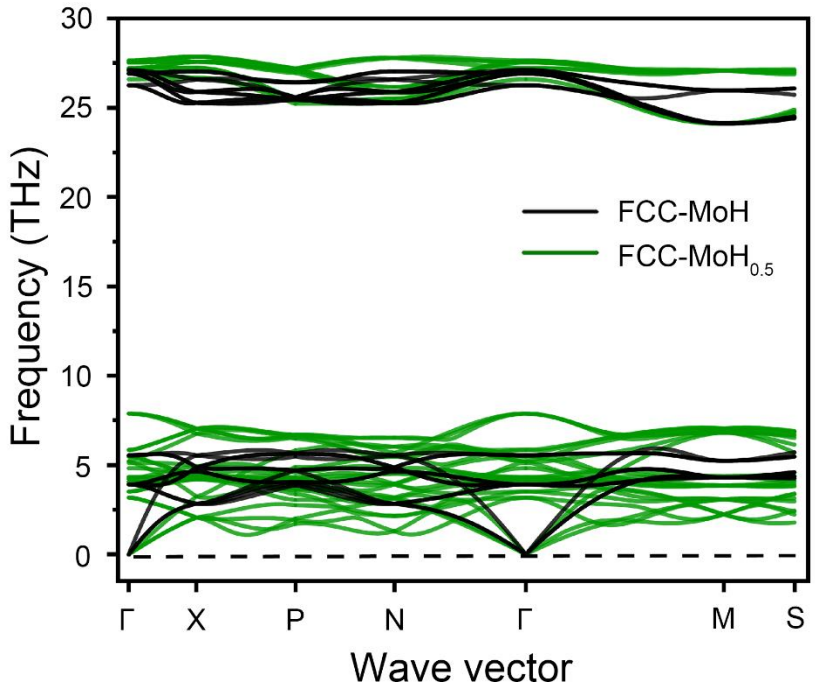

Supplementary Fig. 13 Phonon dispersion spectra of FCC-MoH$_x$ for x = 1.0 and 0.5. The absence of imaginary frequencies confirms the dynamic stability of both structures at these H concentrations. The overall downward shift of phonon branches in $MoH_{0.5}$ indicates phonon softening with reduced H content. This softening signifies that the reduction of H atoms weakens the interatomic force constants and reduces the dynamic stability of the FCC lattice, implying that the structure will eventually become unstable as the H concentration further decreases.

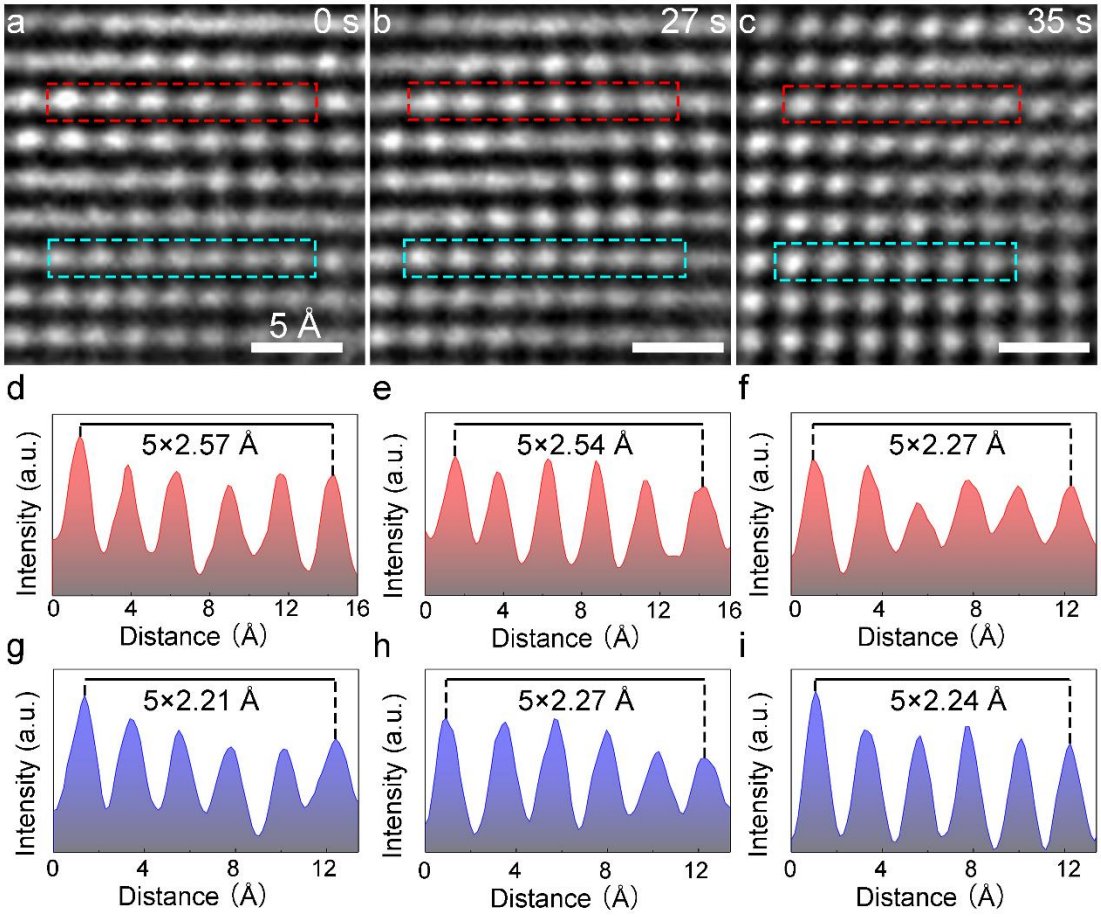

Supplementary Fig. 14 Strain response during the FCC-to-BCC phase transformation. a-c, Sequential HRTEM images showing the phase transition process. **d-i,** Profiles of the interatomic spacing in the FCC (pink) and adjacent BCC (blue) phases. The data reveal strain relaxation in the BCC phase, as evidenced by the decrease in its lattice spacing from 2.27 Å to 2.24 Å.

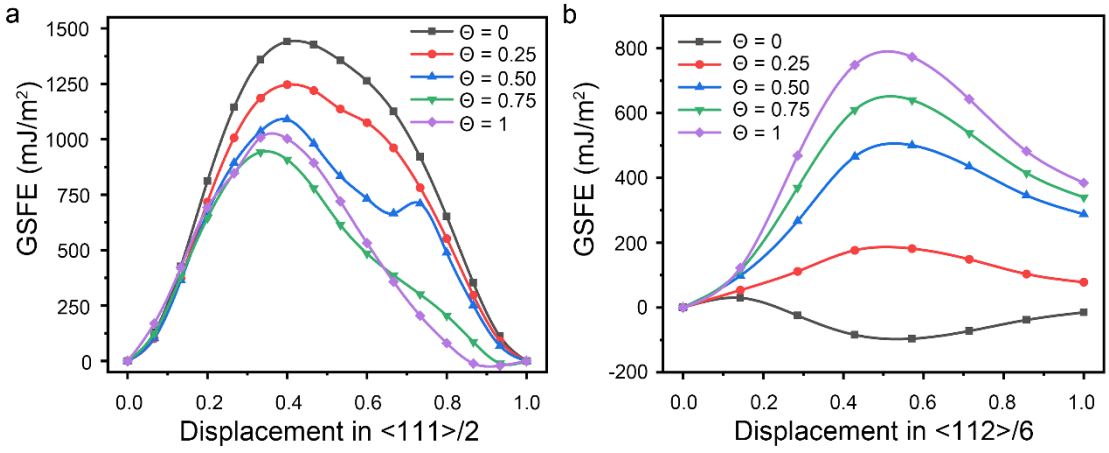

Supplementary Fig. 15 The GSFE curves of BCC and FCC Mo at different *Θ*. a,

GSFE curves for the 1/2<111>{112} slip system in the BCC structure, which has the highest Schmid factor of 0.47 under the [011] tensile loading direction. **b,** GSFE curves for 1/6<112>{111} slip system in the FCC structure. Note that at Θ = 0, the energy profile becomes negative, indicating the mechanical instability of the FCC Mo lattice in the absence of hydrogen.

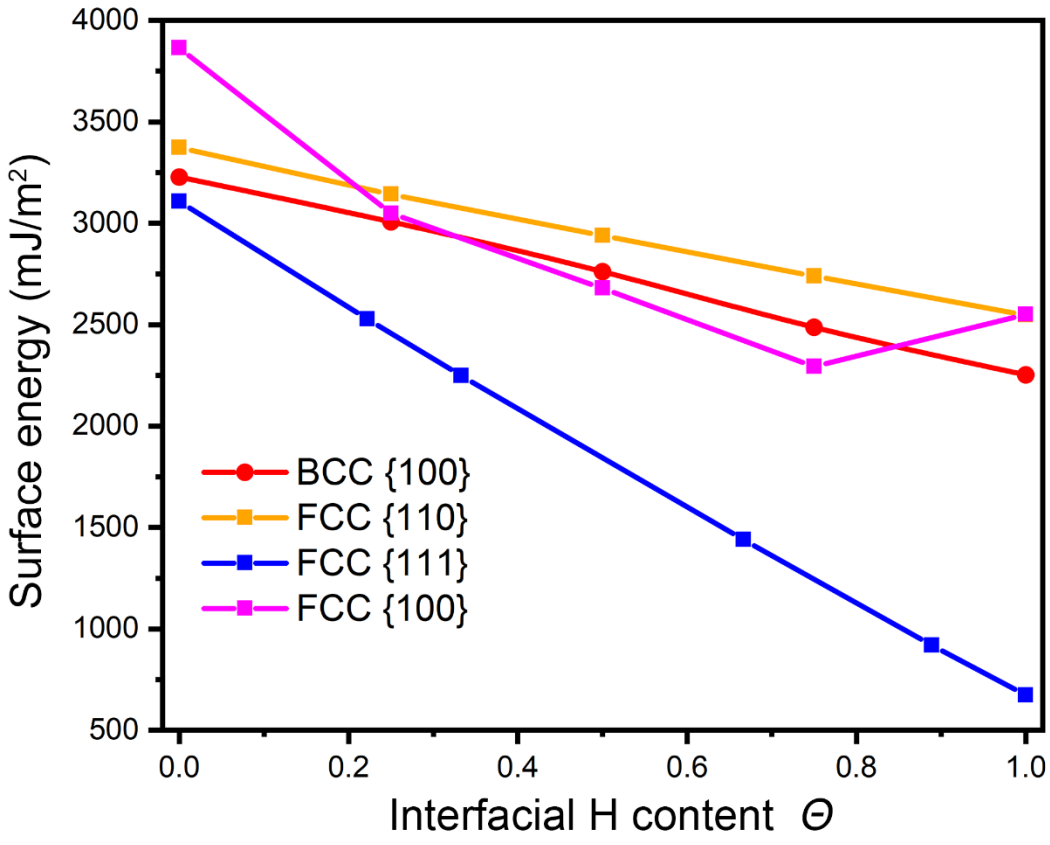

Supplementary Fig. 16 Calculated surface energies for BCC and FCC Mo as a function of Θ. Due to the disparities in the spatial arrangement of interstitial sites among these crystallographic planes, the Θ values employed for the FCC {111} surface differ from those used for other planes.

Description of Additional Supplementary Files

File Name: Supplementary Movie 1
Description: Electromigration and fracture of a Mo NW under high-density electrical current. Played at 8× speed.

File Name: Supplementary Movie 2
Description: The process of BCC-to-FCC phase transformation on the surface of the BCC Mo NW induced by e-beam irradiation. Played at 64× speed.

File Name: Supplementary Movie 3
Description: Deformation of a [011]-oriented dual-phase Mo NW subjected to tension. Played at 4× speed.

File Name: Supplementary Movie 4
Description: Deformation of a [011]-oriented single-phase Mo NW subjected to tension. Played at 4× speed.

File Name: Supplementary Movie 5
Description: The process of discrete, two-step FCC-to-BCC phase transformation during tensile deformation. Played at 4× speed.

References

1. Phillipp, F., Saile, B., Schmid, H. & Urban, K. Energy and orientation dependence of atom displacement in BCC metals studied by high-voltage electron microscopy. *Phys. Lett. A* **73**, 123-126 (1979).
2. Wang, Y., Wakasugi, T., Isobe, S., Hashimoto, N. & Ohnuki, S. Interaction of electrons with light metal hydrides in the transmission electron microscope. *J. Electron Microsc.* **63**, 437-447 (2014).
3. Feng, X., Zhang, J., Liu, H., Iitaka, T., Yin, K. & Wang, H. High pressure polyhydrides of molybdenum: A first-principles study. *Solid State Commun.* **239**, 14-19 (2016).
4. Fisher, S. On the temperature rise in electron irradiated foils. *Radiat. Eff.* **5**, 239-243 (1970).
5. Peng, H. et al. Orientation-dependent ductility and deformation mechanisms in body-centered cubic molybdenum nanocrystals. *J. Mater. Sci. Technol.* **154**, 107-113 (2023).
6. Wang, S., Wang, H., Du, K., Zhang, W., Sui, M. & Mao, S. Deformation-induced structural transition in body-centred cubic molybdenum. *Nat. Commun.* **5**, 3433 (2014).